Thermoelectric Transport Properties of Sb-doped SnSe₂ Polycrystalline Alloys

Seung Min Kang[1,†], Jong Wook Rho[2,†], Hyungyu Cho[1], Sanghyun Park[1], Joontae Park[1], and Sang-il Kim[1,*]

[1]*Department of Materials Science and Engineering, University of Seoul, Seoul 02504, Republic of Korea*
[2]*School of Nano Materials Engineering, Kyungpook National University, Gyeongsangbuk-do 37224, Republic of Korea*

Abstract: SnSe₂ alloys have been investigated in recent times as potential *n*-type thermoelectric materials. In this study, the thermoelectric transport properties of a series of Sb-doped SnSe₂, $Sn(Se_{1-x}Sb_x)_2$ ($x = 0$, 0.015, 0.03, 0.045, 0.06) alloys are investigated. The electrical conductivity was generally enhanced with Sb doping owing to a large increase in electron concentration. However, the Seebeck coefficient largely decreased with doping. Consequently, the power factor was significantly lower at a low doping of $x = 0.015$, and then began rising as the doping was increased beyond $x = 0.015$. It was found that the density-of-states effective mass and weighted mobility decreased with Sb doping, implying that the electrical transport properties of SnSe₂ were degraded by Sb doping. The total and lattice thermal conductivities gradually decreased due to additional point defect scattering. Thus, the thermoelectric figure of merit declined significantly, from 0.30 of the pristine sample with a low doping of Sb ($x = 0.015$) at 750 K, to 0.18, and then for $x = 0.06$ it gradually recovered to the value of the undoped sample. The thermoelectric quality factor decreased as the Sb doping was increased, implying that Sb doping did not enhance the thermoelectric transport properties, despite the large increase in electron concentration.

1. INTRODUCTION

Thermoelectric materials directly convert waste heat into electricity via the Seebeck effect [1-3]. The performance of thermoelectric materials is evaluated by thermoelectric figure of merit, $zT = \sigma S^2 T/\kappa_{tot}$; here σ, S, T, and κ_{tot} denote the electrical conductivity, Seebeck coefficient, absolute temperature, and total thermal conductivity, respectively [4,5]. The κ_{tot} is the sum of electronic thermal conductivity κ_{elec} and lattice thermal conductivity, κ_{latt}. To achieve a high zT, a high value of σS^2 (power factor) and a low κ_{tot} are required. However, the complex trade-off relation among σ, S, and κ_{elec} hinders enhancing zT of thermoelectric materials. Despite these obstacles, strategies to enhance zT by improving σS^2 via carrier concentration optimization or by reducing κ_{latt} via phonon scattering caused by additional point defects have been attempted for conventional thermoelectric materials, such as Bi₂Te₃- and PbTe-based alloys [6-9].

Recently, metal dichalcogenides have been studied extensively owing to their unique electronic and optical properties [10-12]. Among those, post-transition metal chalcogenides, such as InSe [13], SnSe [14], and SnSe₂ [15-17] have been investigated as promising thermoelectric materials. SnSe₂ has a CdI₂-type layered structure and has attracted considerable attention as a promising *n*-type thermoelectric material [18,19]. However, it has a low carrier concentration, resulting in low values of σS^2 and zT. Thus, the effect of increasing the carrier concentration on zT has been subsequently studied. Ding et al. predicted that a maximum zT of 2.95 at 800 K can be obtained in the a-axis direction with a carrier concentration of 1×10^{20} cm⁻³ [20]. Kim et al. reported that substitutional doping of Br at the Se site in SnSe₂ resulted in a high zT of 0.62 at 750 K, along with an increase in the carrier concentration to approximately 10^{19} cm⁻³ [17].

In this study, we employed Sb as a dopant for Se site in SnSe₂ to increase its carrier (electron) concentration. Choe et

al. reported that Sb doping of the Se site of $SnSe_2$ increased the electron concentration from 7.40×10^{17} to 1.50×10^{19} cm^{-3} significantly; this was facilitated by the donor-like behavior of Sb at the Se site [21]. They found that Sb doping in the Se site provides electrons as Sb doped as metal with the oxidation number almost ~0 based on the Bader net charge distribution analysis [21]. (Note that either Sb^{3+} doping in Sn site of $SnSe_2$ or Sb^{3-} doping in Se site of $SnSe_2$ cannot generate electrons.) Thus, herein, we prepared a series of $Sn(Se_{1-x}Sb_x)_2$ to systematically investigate the influence of Sb doping on the thermoelectric transport properties of $SnSe_2$ to further understand the Sb doping in Se site in $SnSe_2$. It was observed that the electron concentration increased significantly with Sb doping. In addition, the thermoelectric transport properties of the Sb-doped $SnSe_2$ samples were analyzed using density-of-state effective mass, m_d^*, weighted mobility, μ_w, and thermoelectric quality factor, B.

2. EXPERIMENTAL PROCEDURES

Polycrystalline $Sn(Se_{1-x}Sb_x)_2$ samples (x = 0, 0.015, 0.03, 0.045, and 0.06) were synthesized using a solid-state reaction method. Stoichiometric amounts of Sn, Se, and Sb were weighed and vacuum-sealed in a quartz tube. The vacuum-sealed quartz tubes were heat-treated at 1073 K for 8 h, then quenched with cold water, and annealed at 850 K for 72 h. The obtained ingots were pulverized for 5 min by high energy ball milling in an Ar atmosphere. The crystal structures of the powders were characterized by X-Ray diffraction using CuK$_{\alpha1}$ radiation (XRD, D8 Discover, Bruker). XPS analysis were carried out with X-ray spectrometer (Nexsa G2 XPS, Thermo Scientific) using a focused monochromatized Al Kα radiation. The powders were densified via spark plasma sintering at 10^{-6} Torr and 707 K for 10 min. The σ and S values were measured by a thermoelectric evaluation system (ZEM-3M8, Advance Riko, Japan) in the temperature range of 300–790 K. Measuring direction was along the perpendicular direction of SPS pressing direction. The Hall measurement of each sample was performed using a Hall measurement system under a magnetic field of 0.553 T (HMS5300, Ecopia). Thermal diffusivity, α, required to obtain κ$_{tot}$ (κ$_{tot}$ = $\alpha \times \rho_s \times C_p$, where ρ_s and C_p are the sample density and heat capacity,

Table 1. Relative density of sintered samples.

$Sn(Se_{1-x}Sb_x)_2$	Relative density (%)
$x = 0$	96.6
$x = 0.015$	95.4
$x = 0.03$	95.9
$x = 0.045$	95.2
$x = 0.06$	95.1

respectively) was measured by the laser flash method (LFA457, Netzsch) in the temperature range of 300–790 K. Measuring direction was along the perpendicular direction of SPS pressing direction. ρ_s of the samples was calculated by Archimedes` method.

Table 1 shows relative density of sintered samples. Relative density of samples was calculated via dividing ρ_s by theoretical density of hexagonal $SnSe_2$, i.e., 5.950 g/cm^3 [22]. C_p was calculated based on the following empirical relationship [23]: $C_p = 73.39 + 1.15 \times 10^{-2} T - 1.92 \times 10^5 T^2$ J/mol·K. As the doping concentrations of the samples were significantly low, the changes in C_p from the Sb doping were considered negligible. Following the data measurements, zT values were calculated.

3. RESULTS AND DISCUSSION

Fig. 1(a) presents XRD peaks of the pulverized $Sn(Se_{1-x}Sb_x)_2$ samples. The XRD patterns show that the hexagonal $SnSe_2$ samples were synthesized without any additional phases. The lattice parameters were calculated using the (001) and (110) diffraction peaks (Fig. 1(b)); it was observed that there was no significant change in the lattice parameters. Fig. 1(c) shows the XPS spectra of the $Sn(Se_{1-x}Sb_x)_2$ (x = 0 and 0.06) samples, which shows presence of Sn 3d, Se 3d peaks. Fig 1(d) and Fig 1(e) show high resolution XPS peaks of Sn 3d and Se 3d respectively. The XPS peaks of Sn 3d$_{3/2}$, Sn 3d$_{5/2}$, Se 3d$_{3/2}$ and Se 3d$_{5/2}$ are located at 494.0, 485.6, 54.3 and 53.5eV, respectively, which is in good agreement with prior study of polycrystalline $SnSe_2$ [24]. Fig. 1(f) shows high resolution Sb 3d XPS spectra of $Sn(Se_{1-x}Sb_x)_2$ (x = 0.06), which shows presence of Sb peaks. Overlap of the O 1s peak and Sb 3d$_{5/2}$ peak indicates physiosorbed oxygens at the surface. The Sb 3d$_{5/2}$ peak of the Sb-doped $SnSe_2$ sample appears at binding energy of 529.1 eV, which is close
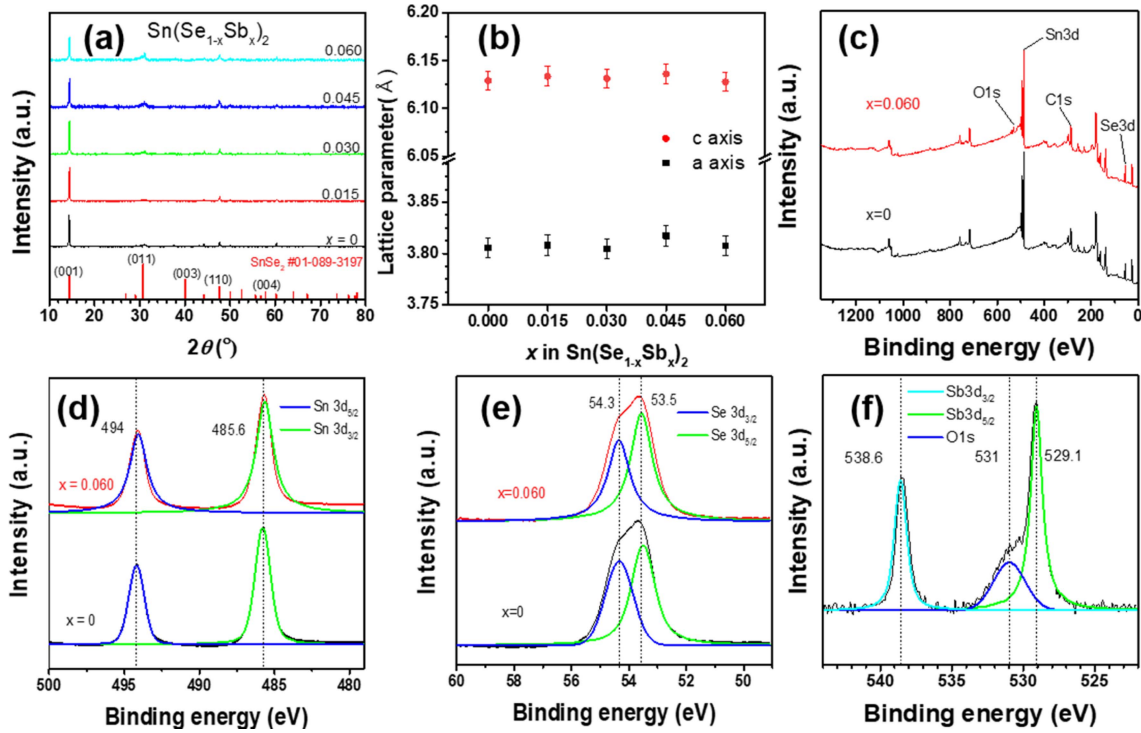
Fig. 1. (a) XRD patterns of $Sn(Se_{1-x}Sb_x)_2$ samples. (b) lattice parameters calculated from XRD data. (c) The XPS spectra of $SnSe_2$ and $Sn(Se_{1-x}Sb_x)_2$ ($x = 0.06$). (d) High resolution Sb3d XPS spectra of the $Sn(Se_{1-x}Sb_x)_2$ ($x = 0.06$).

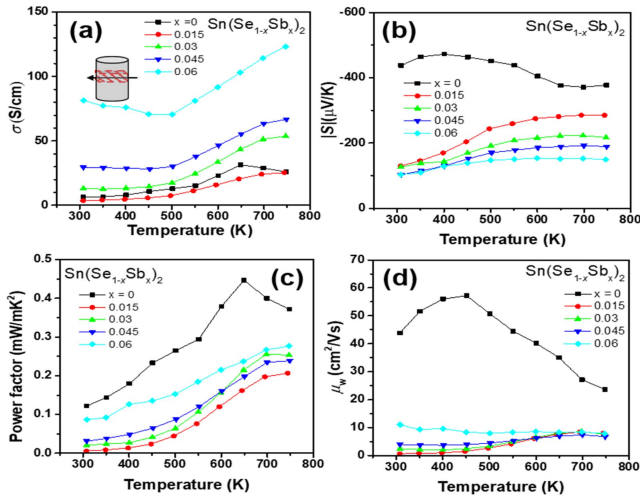**Fig. 2**. (a) Electrical conductivity as a function of temperature for $Sn(Se_{1-x}Sb_x)_2$ samples ($x = 0$, 0.015, 0.03, 0.045, and 0.06). (b) Seebeck coefficient as a function of temperature. (c) Power factor as a function of temperature. (d) Weighted mobility as a function of temperature.

to the binding energy of 528.3 eV of metallic antimony (Sb^0) [25].

Fig. 2(a) and 2(b) show σ and S as functions of temperature. The σ values of the Sb-doped samples increased

with increasing Sb content, except for $x = 0.015$. As shown in Fig. 2(a), the σ values at 300 K for $x = 0$, 0.015, 0.03, 0.045, and 0.06 were 6.35, 3.60, 13.2, 29.5, and 81.4 S/cm, respectively. The values of S of all the samples were negative over whole temperature range, thus establishing the n-type conduction behavior of the samples. The absolute S of the undoped sample ($x = 0$) generally decreased with temperature. In contrast, the absolute S of all the doped samples increased with temperature. At 300 K, the magnitude of S for $x = 0.015$ decreased significantly to –130 µV/K compared with –438 µV/K of the pristine sample. Moreover, the magnitude of S gradually decreased to –127, –103, and –103 µV/K for $x = 0.03$, 0.045, and 0.06, respectively. At 750 K, the S values changed rather gradually to –377, –285, –217, –189, and –150 µV/K for $x = 0$, 0.015, 0.03, 0.045 and 0.06, respectively. Fig. 2(c) shows the calculated power factor σS^2 as a function of temperature for the $Sn(Se_{1-x}Sb_x)_2$ samples. The power factor values of Sb-doped samples decreased compared to that of the pristine sample at all temperatures. Moreover, σS^2 decreased significantly at the low doping level of $x = 0.015$ and
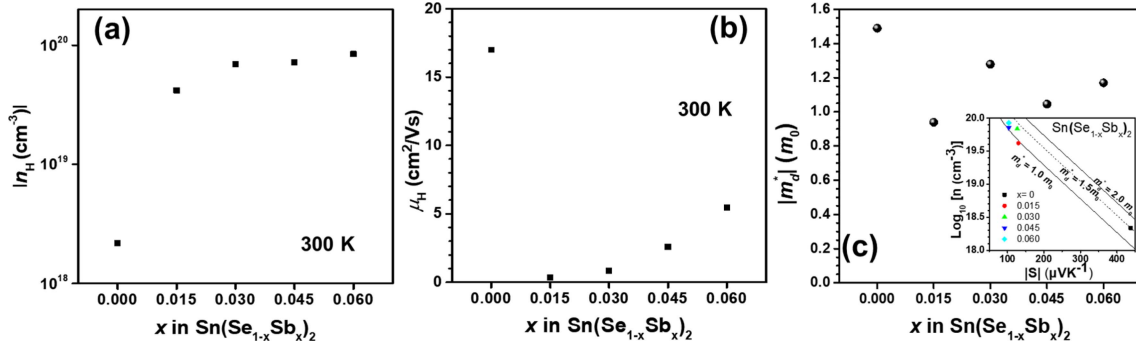
Fig. 3. (a) Hall carrier concentration of $Sn(Se_{1-x}Sb_x)_2$ samples at 300 K. (b) Hall carrier mobility of samples at 300 K. (c) Calculated effective mass (m_d^*) as a function of the Sb doping content (x). The inset of (c) shows $\log_{10} n_H$ as a function of $|S|$ of the samples.

generally increased $x > 0.015$. The significant decrease in σS^2 for $x = 0.015$ could be attributed to the large reduction in the magnitude of S (Fig. 2(b)).

Next, μ_w was calculated and displayed in Fig. 2(d) as a function of temperature. μ_w refers to theoretical maximum power factor that can be obtained by optimizing carrier concentration [26] and can be analytically calculated from the Drude–Sommerfeld free-electron model for $|S| > 20$ μV/K [25]:

$$\mu_w = \frac{3h^3\sigma}{8\pi e(2m_e kT)^{3/2}}$$

$$\left[\frac{\exp\left[\frac{|S|}{k/e}-2\right]}{1+\exp\left[-5\left(\frac{|S|}{k/e}-1\right)\right]} + \frac{\frac{3}{\pi^2}\frac{|S|}{k/e}}{1+\exp\left[5\left(\frac{|S|}{k/e}-1\right)\right]}\right] \quad (1)$$

where h and m_e denote Planck's constant and electron mass, respectively. As shown in Fig. 2(d), μ_w was reduced significantly for the doped samples. For instance, at 300 K μ_w values were 44, 0.69, 2.4, 4.0, and 11 cm²/V·s for $x = 0$, 0.015, 0.03, 0.045, and 0.06, respectively. At 750K, the corresponding values were 23, 8.0, 7.6, 6.8, and 7.9, respectively. The undoped sample had the highest μ_w among all the samples over the entire temperature range, and it increased with increasing Sb doping, following the same trend as σS^2 (Fig. 2(c)).

Fig. 3(a) and 3(b) present Hall carrier concentration, n_H and Hall carrier mobility, μ_H at 300 K for $Sn(Se_{1-x}Sb_x)_2$ as functions of x. The values of n_H were 2.17×10^{18}, 4.17×10^{19}, 6.91×10^{19}, 7.14×10^{19}, and 8.44×10^{19} cm⁻³ for $x = 0$, 0.015, 0.03, 0.045, and 0.06, respectively. Furthermore, n_H

increased significantly at the low doping level of $x = 0.015$ and gradually increased for x beyond 0.015. This result indicates that the Sb metal with the oxidation number ~0 doped into the anion site of $SnSe_2$ so Sb^0 in Se^{2-} site acts as an electron donor, which is reported in ref. [21] based on the Bader net charge calculations. The small difference of electronegativity and long bond length between Sn and Sb hindered the effective charge transfer of the Sn–Sb bond, which could validate the oxidation number of the Sb atoms to become approximately 0, which is known from Bader net charge calculation [21]. Thus, the Sb in Se sites in our samples of $Sn(Se_{1-x}Sb_x)_2$ behaves as electron donors.

As shown in Fig. 3(b), μ_H was significantly reduced for the doped samples (0.36, 0.86, 2.6, and 5.5 cm²/Vs for $x = 0.015$, 0.03, 0.045, and 0.06, respectively), as compared with 17 cm²/Vs for the undoped sample. The large reduction of μ_H is also seen for $Sn(Se_{0.96}Sb_{0.04})_2$ composition. in ref [21].

Fig. 3(c) shows the calculated m_d^* of $Sn(Se_{1-x}Sb_x)_2$ samples based on a single parabolic band model under the acoustic phonon scattering mechanism [27]:

$$\log_{10}\left(\frac{m_d^* T}{300}\right) = \frac{2}{3}\log_{10}(n)$$

$$-\frac{2}{3}[20.3 - (0.00508 \times |S|) + (1.58 \times 0.967^{|S|})] \quad (2)$$

where m_d^* and n denote the effective density-of-state mass and carrier concentration, respectively. The inset graph of Fig. 3(c) shows logarithmic n_H as a function of $|S|$. The m_d^* values of the doped samples were 0.94, 1.28, 1.05, and 1.17 m_0 for $x = 0.015$, 0.03, 0.045, and 0.06, respectively; these were lower than 1.48 m_0 for $x = 0$. Both m_d^* and μ_w (Fig.
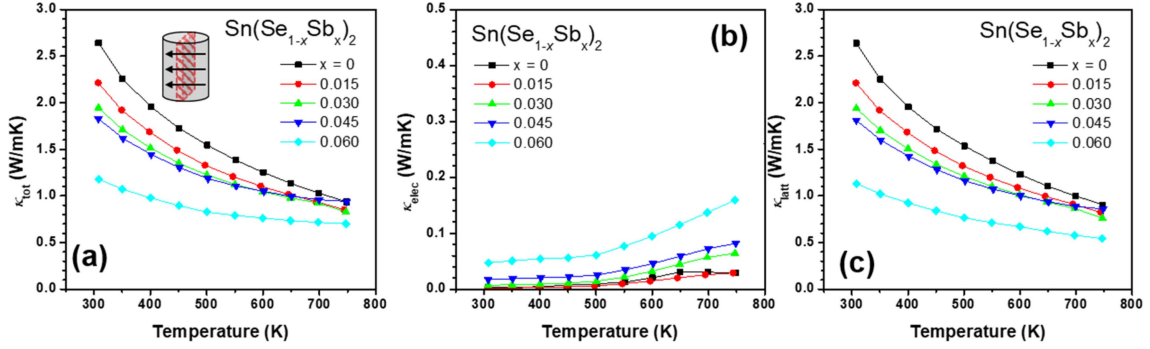
Fig. 4. (a) Total thermal conductivity, (b) electrical thermal conductivity, and (c) lattice thermal conductivity as a function of temperature for Sn(Se$_{1-x}$Sb$_x$)$_2$ samples.

2(d)) decreased with Sb doping, suggesting that the electrical transport properties were degraded by Sb doping in SnSe$_2$.

Fig. 4(a), 4(b), and 4(c) present κ_{tot}, κ_{elec}, and κ_{latt}, respectively. κ_{elec} of the samples was calculated using the Wiedemann–Franz law [28] as follows: $\kappa_{elec} = L\sigma T$, where L denotes the Lorenz number and is calculated using the following equation [29]:

$$L = 1.5 + \exp\left(-\frac{|S|}{116}\right) \tag{3}$$

κ_{latt} is obtained by subtracting κ_{elec} from κ_{tot}. As the measured κ_{elec} of the samples was extremely small owing to low σ values, κ_{latt} was nearly equal to κ_{tot}. The values of κ_{latt} of the doped samples were 2.64, 2.21, 1.94, 1.81, and 1.13 W/mK at 300 K and 0.91, 0.82, 0.76, 0.86, and 0.54 W/mK at 750 K for $x = 0$, 0.015, 0.03, 0.045, 0.06, respectively. Moreover, κ_{latt} noticeably decreased with doping, indicating that Sb doping increased point defect scattering.

Fig. 5(a) shows the calculated zT values as functions of temperature. In general, no noticeable zT enhancement was observed upon doping. zT was decreased significantly by low-level doping of Sb ($x = 0.015$); then, for $x = 0.06$. zT gradually recovered to the value of the undoped sample. The large reduction in zT could be attributed to the large reduction in σS^2; moreover, the gradual increase in zT beyond $x = 0.15$ was owing to the modest recovery of σS^2 (Fig. 2(c)) and the reduction in the thermal conductivities (Fig. 4(a) and 4(c)). No enhancement of zT could be achieved in the Sb-doped Sn(Se$_{1-x}$Sb$_x$)$_2$ samples in the x range of 0.015–0.06. Fig 5(b) shows B of each sample, which was calculated using the following equation [30]:
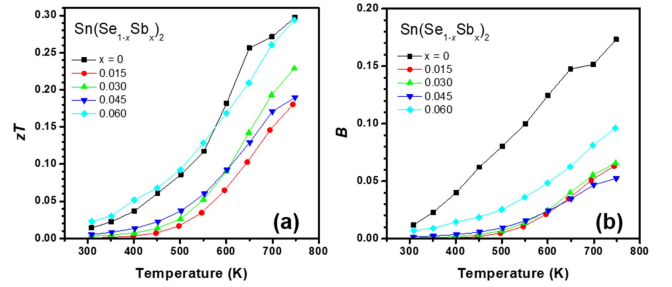

Fig. 5. (a) Thermoelectric figure of merit as a function of temperature for Sn(Se$_{1-x}$Sb$_x$)$_2$ samples. (b) Quality factor B as a function of temperature.

$$B = \left(\frac{k}{e}\right)^2 \frac{8\pi e (2m_e kT)^{3/2}}{3h^3} \cdot \frac{\mu_w}{k_{latt}} T . \tag{4}$$

B is proportional to maximum zT when n_H is optimized. The values of B for $x = 0$, 0.015, 0.03, 0.045, and 0.06 were 0.0120, 0.0002, 0.0009, 0.0016, and 0.0070, respectively at 300 K and 0.170, 0.060, 0.066, 0.052, and 0.096, respectively at 750 K. Generally, B of Sb-doped sample was lower than that of pristine SnSe$_2$. Sb doping in SnSe$_2$ successfully and significantly increased the electron concentration, and reduced the thermal conductivities; however, the overall thermoelectric transport properties were not enhanced owing to reduction of m_d^* and μ_w.

4. CONCLUSIONS

In this study, a series of Sn(Se$_{1-x}$Sb$_x$)$_2$ ($x = 0$, 0.015, 0.03, 0.045, and 0.06) polycrystalline samples was synthesized and their thermoelectric transport properties were investigated. Electrical conductivity was generally enhanced by Sb doping owing to a large increase in the electron concentration; in

contrast, the Seebeck coefficient was largely decreased by doping. Consequently, the power factor for the lowest doping (x = 0.015) was significantly decreased from 0.37 mW/mK^2 of the pristine samples at 600 K to 0.21 mW/mK^2. The power factor generally increased as the Sb doping increased from x = 0.015. The density-of-state effective mass and weighted mobility decreased with Sb doping, suggesting that the electrical transport properties were consequently degraded by Sb doping in SnSe$_2$. The total and lattice thermal conductivities gradually decreased owing to additional point defect scattering. Thus, thermoelectric figure of merit at the lowest Sb doping (x = 0.015) decreased significantly from 0.30 of the pristine sample at 750 K to 0.18; subsequently, the thermoelectric figure of merit gradually recovered to the value of the undoped sample at x = 0.06. The thermoelectric quality factor decreased as the Sb doping increased. Sb doping in SnSe$_2$ significantly enhanced the electron concentration and reduced the thermal conductivities; however, the overall thermoelectric transport properties were not enhanced owing to a reduction in the density-of-state effective mass and weighted mobility.

ACKNOWLEDGEMENT

REFERENCES

1. G. D. Mahan, and J. O. Sofo, *Proc. Natl. Acad. Sci.* **93**, 7436 (1996).

2. F. J. DiSalvo, *Science* **285**, 703 (1999).

3. G. J. Snyder and S. T. Eric, *Nat. mater.* **7,** 105 (2008).

4. M. W. Gaultois, T. D. Sparks, C. K. Borg, R. Seshadri, W. D. Bonificio, and D. R. Clarke, *Chem. Mater.* **25**, 2911 (2013).

5. T. M. Tritt, and M. A. Subramanianm, *MRS bull.* **31**, 188 (2006).

6. O. Park, T. Kim, M. Heo, S. J. Park, S. W. Lee, H. K. Cho, and S. I. Kim, *Korean J. Met. Mater.* **61.** 206 (2023).

7. D. H. Kim, H. S. Kim, S. Hong, J. H. Lee, J. G. Han, H. S. Cho, S. W. Lee, and S. I. Kim, *Electron. Mater. Lett.* **17**, 443 (2021).

8. Y. S. Lim, B. G. Park, and G. -G. Lee, *Korean J. Met. Mater.* **60,** 463 (2022).

9. R. J. Korkosz, T. C. Chasapis, S. H. Lo, J. W. Doak, Y. J. Kim, C. I. Wu, E. Hatzikraniotis, T. P. Hogan, D. N. Seidman, C. Wolverton, V. P. Dravid, and M. G. Kanatzidis, *J. Am. Chem. Soc.* **136**, 3225 (2014).

10. Q. H. Wang, K. Kalantar-Zadeh, A. Kis, J. N. Coleman, and M. S. Strano, *Nat. Nanotechnol.* **7**, 699 (2012).

11. S. Manzeli, D. Ovchinnikov, D. Pasquier, O. V. Yazyev, and A. Kis, *Nat. Rev. Mater.* **2**, 1 (2017).

12. O. Park, T. W. Kim, S. W. Lee, H. -S. Kim, W. H. Shin, J. U. Rahman, S. -i. Kim, *Korean J. Met. Mater.* **60**, 315 (2022).

13. K. H. Lee, M. W. Oh, H. S. Kim, W. H. Shin, K. Lee, J. H. Lim, J. I. Kim, and S. I. Kim, *Inorg. Chem. Front.* **6**, 1475 (2019).

14. C. L. Chen, H. Wang, Y. Y. Chen, T. Day, and G. J. Snyder, *J. Mater. Chem. A.* **2**, 11171 (2014).

15. D. S. Hyeon, M. S. Oh, J. T. Kim, Y. J. Lee, S.I. Kim, S. P. Moon, N. Hamayoun, S. W. Kim, K. H. Lee, J. Bang, and K. Lee, *J. Phys. D* **51**, 455102 (2018).

16. S. I. Kim, S. Hwang, S. Y. Kim, W. J. Lee, D. W. Jung, K. S. Moon, H. J. Park, Y. J. Cho, Y. H. Cho, J. H. Kim, D. J. Yun, K. H. Lee, I. Han, K. Lee, and Y. Sohn *Sci. Rep.* **6**, 19733 (2016).

17. S. I. Kim , J. Bang, J. An , S. Hong , G. Bang , W. H. Shin , T. W. Kim , K. Lee, *J. Alloys Compd.* **868**, 159161 (2021).

18. S. Wu, H. Yang, Z. Wu, C. Liu, L. Miao, J. Gao, X. Wang, X. Wang, C. Shen, J. G. Noudem, and J. Wang, *ACS Appl. Energy Mater.* **2**, 8481 (2019).

19. F. Li, Z. Zheng, Y. Li, W. Wang, J. F. Li, B. Li, A. Zhong, J. Luo, and P. Fan, *J. Mater. Sci.* **52**, 10506 (2017).

20. Y. Ding, B. Xiao, G. Tang, and J. Hong, *J. Phys. Chem. C* **121**, 225 (2017).

21. J. S. Choe, C. Lee, M. J. Kim, G. G. Lee, J. H. Shim, and Y. S. Lim, *J. Appl. Phys.* **127**, 185706 (2020).

22. G. Busch, C. Fröhlich, F Hulliger, and E. Steigmeier, *Helv. Phys. Acta.* **34**, 359(1961).

23. H. Wiedemeier, G. Pultz, U. Gaur, and B. Wunderlich, Thermochim. Acta. **43**, 297 (1981).

24. S. Wu, C. Liu, Z. Wu, L. Miao , J. Gao , X. Hu, J. Chen, Y. Zheng, X. Wang, C. Shen, H. Yang, and X. Zhou, *Ceram. Int.* **45**, 1 (2019).

25. C. Jill. and R. C. King Jr. *Handbook of X-ray photoelectron spectroscopy*, p 221, Perkin-Elmer Corp, US (1992).

26. M. Kim, S. I. Kim, S. W. Kim, H. S. Kim, and K. H. Lee, *Adv. Mater.* **33**, 2005931 (2021).

27. G. J. Snyder, A. H. Snyder, M. Wood, R. Gurunathan, B. H.

Snyder, C. Niu, *Adv Mater.* **32**, 2001537 (2020).

28. K. H. Lee, S. Kim, J. Lim, J. Y. Cho, H. Yang, and H. Kim, *Adv. Funct. Mater.* **32**, 2203852 (2022).

29. H. S. Kim, Z. M. Gibbs, Y. Tang, H. Wang, and G. J. Snyder,

APL Mater. **3**, 041506 (2015).

30. Y. Pei, H. Wang, and G. J. Snyder, *Adv Mater.* **24**, 6125 (2012).